

# Journal of Materials Chemistry C

Accepted Manuscript



This is an *Accepted Manuscript*, which has been through the Royal Society of Chemistry peer review process and has been accepted for publication.

*Accepted Manuscripts* are published online shortly after acceptance, before technical editing, formatting and proof reading. Using this free service, authors can make their results available to the community, in citable form, before we publish the edited article. We will replace this *Accepted Manuscript* with the edited and formatted *Advance Article* as soon as it is available.

You can find more information about *Accepted Manuscripts* in the [Information for Authors](#).

Please note that technical editing may introduce minor changes to the text and/or graphics, which may alter content. The journal's standard [Terms & Conditions](#) and the [Ethical guidelines](#) still apply. In no event shall the Royal Society of Chemistry be held responsible for any errors or omissions in this *Accepted Manuscript* or any consequences arising from the use of any information it contains.

## Mechanism of chemical doping in electronic-type-separated single wall carbon nanotubes towards high electrical conductivity

Ivan Puchades, Colleen C. Lawlor, Christopher M. Schauerman, Andrew R. Bucossi, Jamie E. Rossi, Nathanael D. Cox, Brian J. Landi\*

Rochester Institute of Technology, 1 Lomb Memorial Drive, Rochester, NY 14623, USA.

*KEYWORDS* single wall carbon nanotubes, electronic-type separated SWCNTs, carbon nanotube doping, redox potential of carbon nanotubes, doping stability

**ABSTRACT** Enhanced electrical conductivity of carbon nanotubes (CNTs) can enable their implementation in a variety of wire and cable applications traditionally employed by metals. Electronic-type-separated single wall carbon nanotubes (SWCNTs) offer a homogeneous platform to quantify the unique physiochemical interactions from different chemical dopants and their stability. In this work, a comprehensive study of chemical doping with purified commercial CNT sheets shows that I<sub>2</sub>, IBr, HSO<sub>3</sub>Cl (CSA) and KAuBr<sub>4</sub> are the most effective at increasing the electrical conductivity of CNT films by factors between 3x and 8x. These dopants are used with electronic-type-separated SWCNT thin-films to further investigate changes in SWCNT optical absorption, Raman spectra, and electrical conductivity. The dopant effects with semiconducting SWCNTs result in quenching of the S<sub>11</sub> and S<sub>22</sub> transitions, and a red shift of 8-10 cm<sup>-1</sup> of the Raman G' peak, when compared to a purified SWCNT thin-film. The average electrical conductivity of purified semiconducting SWCNT thin-films is 7.3×10<sup>4</sup> S/m. Doping

increases this conductivity to  $1.9 \times 10^5$  S/m for CSA (2.6x increase),  $2.2 \times 10^5$  S/m for IBr (3.1x), to  $2.4 \times 10^5$  for  $I_2$  (3.3x), and to  $4.3 \times 10^5$  for  $KAuBr_4$  (5.9x). In comparison, metallic SWCNT thin-films exhibit only slight quenching of the optical absorbance spectra for the  $M_{11}$  transition, and shifts in the Raman G'-peak of less than  $1 \text{ cm}^{-1}$  for  $I_2$  and IBr, whereas  $KAuBr_4$  and CSA promote red shifting by  $4 \text{ cm}^{-1}$ , and  $7 \text{ cm}^{-1}$ , respectively, when compared to a purified control sample. The increase in electrical conductivity of metallic SWCNT thin-films is gradual and depends on the dopant. With an average value of  $9.0 \times 10^4$  S/m for the purified metallic SWCNT thin-films,  $I_2$  doping increases the electrical conductivity to  $1.0 \times 10^5$  (1.1x increase), IBr to  $1.5 \times 10^5$  S/m (1.7x),  $KAuBr_4$  to  $2.4 \times 10^5$  S/m (2.6x), and CSA to  $3.2 \times 10^5$  S/m (3.5x). The time-dependent stability of the chemical dopants with SWCNTs is highest for  $KAuBr_4$ , which remains in effect after 70 days in ambient conditions. The doping-enhanced electrical conductivity is attributed to the relative potential difference between the SWCNT electronic transitions and the redox potential of the chemical species to promote charge transfer. The results of this work reinforce the chemical doping mechanism for electronic-type-separated SWCNTs and provide a path forward to advance SWCNT conductors.

## I. Introduction

Carbon nanotubes (CNTs) are currently being considered as a viable alternative to conventional conductor materials, such as copper and aluminum, due to their intrinsic mechanical and electrical properties. Enhanced flexural tolerance and environmental stability of bulk CNT materials have been demonstrated with CNT wires, withstanding greater than 200,000 bending cycles and 80 days in a corrosive environment without increasing resistivity.<sup>1</sup> Steady progress to improve the electrical conductivity has been underway since the theoretical conductivity of

defect-free, individual single wall carbon nanotubes (SWCNTs) ( $1 \times 10^8$  S/m) was determined to be higher than that of bulk copper ( $5.8 \times 10^7$  S/m).<sup>1</sup> However, the highest empirical conductivity value for a bulk CNT material to date at room temperature is markedly lower at  $\sim 5 \times 10^6$  S/m.<sup>2</sup>

There are several prevalent methods being evaluated to improve the electrical conductivity of CNT wires and films. For example, CNT alignment, diameter and length are all reported to affect the electrical conductivity of CNT networks.<sup>3-8</sup> Chemical doping methods<sup>10-24</sup> have also been shown to increase the conductivity of CNTs by both reducing the barrier for conduction between CNTs in the network (inter-tube junctions) and by increasing the number of carriers available for conduction through charge transfer (intra-tube junctions).<sup>17-19</sup>

Recent advancements in separation techniques have allowed for a better understanding of the conduction mechanism of metallic vs. semiconducting SWCNTs.<sup>9</sup> Chemical doping of electronic-type-separated SWCNTs via redox dopants has shown that semiconductor-enriched films can be more effectively doped than metallic-enriched films due to a larger increase in delocalized carrier density, thus reducing tube-tube junction resistance.<sup>17,19,24</sup> Other investigations have been carried out on SWCNT thin-film networks with optoelectronic applications and have exclusively used  $\text{NHO}_3$  and  $\text{SOCl}_2$  as dopants due to their high redox potentials. The opportunity to align the redox potential of a chemical dopant to impact the density of states for varying diameter SWCNTs has been theoretically predicted, and supported by results on unsorted SWCNT thin-films.<sup>20</sup> However, no studies to date have methodically measured the effects of chemical doping across a range of redox potentials in phase pure semiconducting and metallic SWCNTs.

This work presents the first study to utilize electronic-type-separated SWCNTs to selectively probe the interactions between a series of chemical dopants with increasing electrochemical

redox potential in order to modulate effects of doping on charge transfer. Based on an initial survey of more than 40 chemical dopants, I<sub>2</sub>, IBr, chlorosulfonic acid (CSA) and KAuBr<sub>4</sub> are down selected to investigate the conductivity improvements of electronic-type-separated bulk SWCNT networks and provide insight on which type of dopant is more stable under various atmospheric conditions. The SWCNT:dopant interaction is characterized using spectroscopy techniques, including optical absorbance and Raman, as well as electrical conductivity measurements on the same samples. Dopant efficacy in each of the electronic-type-separated SWCNT thin-films is determined using qualitative analysis of relative suppression in optical spectra, and quantitatively based on analysis of the effects on the Raman G'-band. The findings support a mechanism of doping based on electrochemical redox theory and represent important design strategies towards enhancing the conductivity of bulk CNT wire and film structures.

## II. Experimental

Commercially available carbon nanotube (CNT) sheets from Nanocomp Technologies, Inc. (NCTI) were used to perform the initial study of 43 different chemical dopants and their effect on conductivity. These CNTs were selected due to their lower cost availability compared to electronic-type-separated SWCNTs, and serve as a representative material that can be extended to SWCNTs. A three-step purification procedure was used on the CNT sheets to (1) remove amorphous carbon impurities by thermal oxidation in air at 520 °C, (2) remove Fe catalyst impurities by dissolution in concentrated HCl for 30 minutes, and (3) dry the sheets at 500 °C for 10 minutes in air to remove any residual HCl based upon the previously published procedure.<sup>25</sup> Dopants were introduced by soaking 5 mm × 5 mm CNT sheets in a 5 mM dopant solution at room temperature for 30 minutes, followed by a 15 minute, 100 °C vacuum oven dry. All of the dopants listed in Figure 1 were dissolved in water with the exception of 1-Pyrenebutyric acid,

dissolved in methanol, and 1, 2-Dichlorophenoxyacetic acid and 4-Bromoaniline, dissolved in ethanol. Iodine doping was performed at  $\sim 100$  °C by exposing the CNT sheet to iodine vapor for 2 hours. Electrical conductivity of the CNT sheets before and after doping for each condition was measured by 4-point probe and the thickness determined using a calibrated caliper to be  $20 \pm 5$   $\mu\text{m}$ . The measurements were repeated on three separate CNT samples for each dopant, and the results averaged.

Commercially available NanoIntegris SWCNT materials were used to fabricate semiconducting (referred to as “semi”, Iso-Nanotubes-S, 99%), mixed (referred to as “mixed”, Ultra-Pure SWNTs, 99%), and metallic (referred to as “metallic”, Iso-Nanotubes-M, 98%) SWCNT thin-films. The SWCNT thin-films were fabricated based on a previously reported procedure by dispersing  $\sim 0.1$  mg of SWCNTs in 15 mL of chlorosulfonic acid (CSA).<sup>12</sup> The SWCNTs were mixed in a Resodyn LabRAM mixer for 60 minutes at an acceleration of  $10.7 \text{ m/s}^2$ , and were subsequently collected by vacuum filtration on an Anodisc<sup>TM</sup> membrane (Whatman,  $0.02 \mu\text{m}$  pore size, 47 mm outer diameter). The SWCNT thin-films were dried on the filtration apparatus for  $> 6$  hours. The as-produced SWCNT thin-films were released from the membrane by immersion in a deionized (DI) water bath and transferred to a glass slide where they were divided into four equal sections of approximately  $20 \text{ mm} \times 20 \text{ mm}$ , and released by immersion in a DI water bath and transferred to four separate glass slides for characterization. The resulting physical properties for one sample from each electronic-type-separated SWCNT thin-film was characterized with optical absorbance spectroscopy (Perkin Elmer Lambda 900) and Raman spectroscopy (JY Horiba HR800 LabRam, 632.82 nm laser excitation). A mixed SWCNT thin-film was prepared via a film-transfer method based on a mixed cellulose ester (MCE) membrane,<sup>26,27</sup> to serve as the control for optical absorbance measurements. The

SWCNT film thickness was measured using a Veeco Wyko NT1100 optical profiler with white light interferometry. The sheet resistance was measured using an in-line 4-point probe method, with probe spacing of 1.57 mm, and assuming a semi-infinite sample size (20 mm × 20 mm).<sup>28</sup> Reported electrical conductivity values are based on the measured average film thickness and sheet resistance measurements.

Doping susceptibility measurements were performed as a function of SWCNT electronic-type and dopant for SWCNT samples after purification of the as-produced thin-film (*i.e.*, removal of residual impurities/CSA) via thermal oxidation in air. One sample from each SWCNT electronic-type was doped for 1 hour with the following: (1) 10 mM KAuBr<sub>4</sub> in DI water, (2) I<sub>2</sub> vapor in a sealed container at 100 °C with air ambient, and (3) 0.36 M IBr in ethanol. All doping chemicals were purchased from Sigma Aldrich. The KAuBr<sub>4</sub> samples were rinsed with 10mL of DI water and the IBr samples with 10 mL of ethanol to remove any excess solution from the surface of the film and allowed to dry in air at 18-20 °C for 30 minutes. After doping, all SWCNT films were characterized with optical absorbance spectroscopy, Raman spectroscopy, optical profilometry and 4-point probe sheet resistance measurements. Doped SWCNT thin-films were stored under ambient room conditions (Temperature=18-20 °C, Relative Humidity=20-40%) for 70 days while performing spectroscopy and four-point probe measurements to assess the time-dependent dopant stability in the SWCNT thin-films.

### III. Results

Purified NCTI CNT sheets were used to assess the effect of chemical dopant type on electrical conductivity. Reported electrical conductivities of bulk CNT materials can be affected by unintentional dopants either due to functionalization during purification, type separation, or impurities from dispersion and processing,<sup>17,29,30</sup> therefore, maintaining a high purity reference

sample for all relative comparisons is essential. Figure 1(a)-(c) details the effectiveness of the purification process for removing both carbonaceous and metal catalyst impurities from the commercial material based upon the presented SEM images. Conductivity measurements for each purified sample prior to doping are shown in Figure 1(d) and consistency across samples is evident, with some minor variations attributed to density differences post-purification. An increase in CNT electrical conductivity is evident after doping with all chemical species surveyed, however the alkali gold halides, gold halides, and halides exhibit the largest change in electrical conductivity: up to an 8x increase. In the case of the noble metal halides, there exists a tradeoff between the increase in electrical conductivity and the loss of mass savings that is associated with surface plating from reduction of noble metals.<sup>1,16</sup> Therefore,  $\text{KAuBr}_4$  is chosen for SWCNT thin-film studies as representative of the alkali gold halide and gold halide dopants as it exhibits the least amount of plating and consistently has the highest electrical conductivity. Chlorosulfonic acid (CSA) is not included in the survey in Figure 1 due to the incompatibility of exposing CNT sheets without significant physical changes due to the strong interactions toward dispersion. However, since CSA is the dispersion solvent used to fabricate the SWCNT thin-films, and previous results show significant enhancement in the electrical conductivity,<sup>2</sup> it is chosen as representative of the acid dopants. Both of the halides ( $\text{I}_2$  and  $\text{IBr}$ ) are included in the SWCNT thin-film study due their significant increase in electrical conductivity and interest from recent publications on the use of halides.<sup>13-15</sup> Representative chemicals from the other classes including metal nitrates, metal halides, bases, and ionic liquids were not explored further as dopants since they result in lower relative improvements in conductivity.

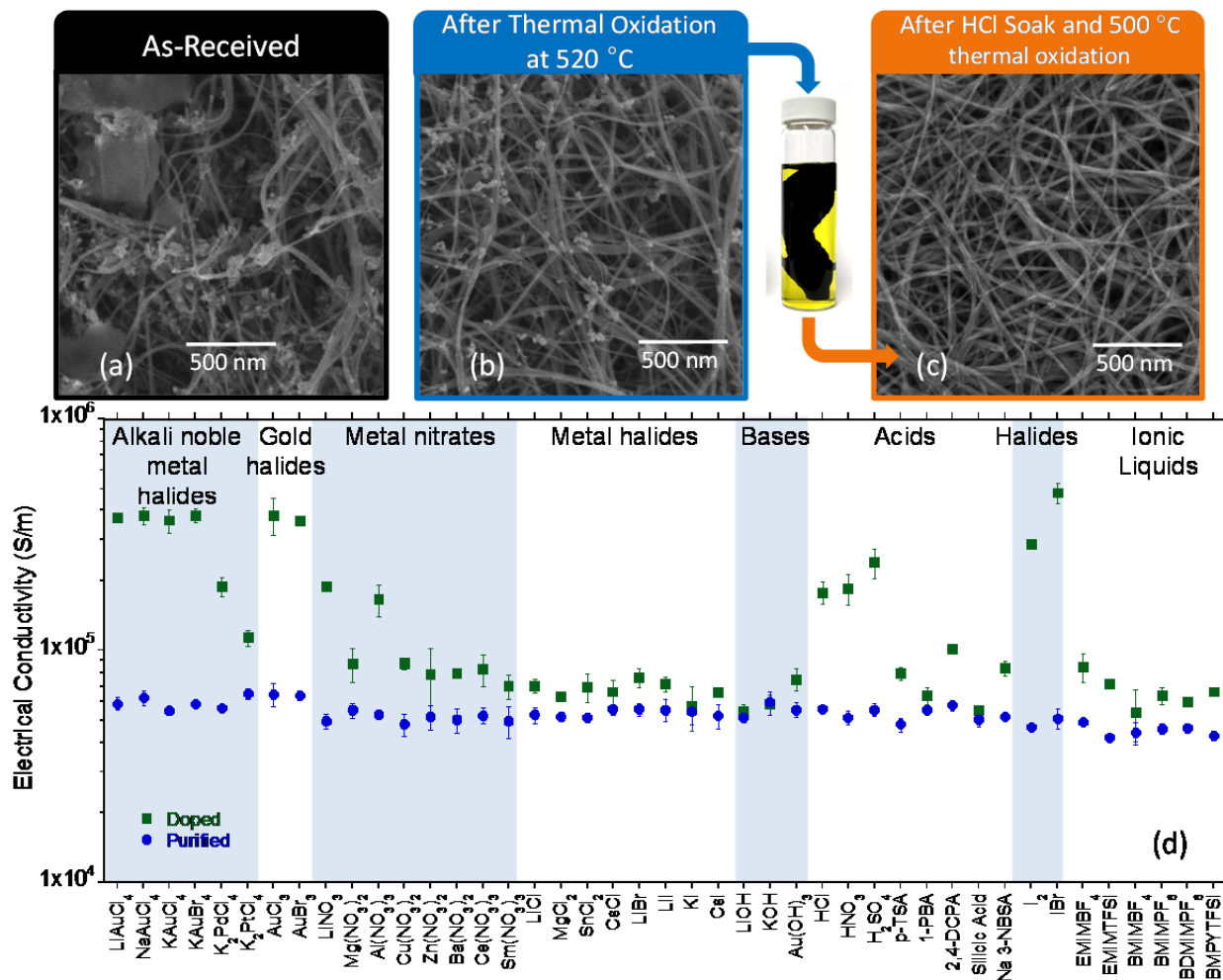


Figure 1. SEM analysis is provided for (a) the as-received NCTI CNT material, (b) after 560 °C thermal oxidation in air, and (c) after HCl soak and 560 °C thermal oxidation. (d) Electrical conductivity of purified and doped NCTI CNTs as a function of different doping species. Error bars represent standard deviation from 3 replicates. P-TSA: p-Toluenesulfonic acid. 1-PBA: 1-Pyrenebutyric acid. 2,4-DCPA: 2,4-Dichlorophenoxyacetic acid. Na 3-NBSA: 3-Nitrobenzene sulfonic acid sodium salt. EMIMBF<sub>4</sub>: 1-Ethyl-3-methylimidazolium tetrafluoroborate, EMIMTFSI: 1-Ethyl-3-methylimidazolium bis(trifluoromethylsulfonyl)imide. BMIMBF<sub>4</sub>: 1-Butyl-3-methylimidazolium tetrafluoroborate. BMIMPF<sub>6</sub>: 1-Butyl-3-methylimidazolium hexafluoroborate. BDMIMPF<sub>6</sub>: 1-Butyl-2,3-dimethylimidazolium hexafluorophosphate. BMPYTFSI: 1-Butyl-1-methylpyrrolidinium bis(trifluoromethylsulfonyl)imide.

SWCNT thin-films were prepared using electronic-type-separated SWCNTs from NanoIntegris. A SWCNT thin-film fabrication process based on CSA:SWCNT dispersions was selected due to the highly effective nature of CSA to debundle the SWCNTs and make quality, uniform films while simultaneously avoiding surfactants and other small molecules to disperse SWCNTs. However, a procedure was required and developed to remove CSA from as-produced SWCNT thin-films to compare other dopants without negatively affecting the SWCNT structure. Thermal oxidation conditions were optimized to achieve removal of CSA by comparing Raman and optical absorbance spectra of a CSA-prepared, mixed electronic-type-separated SWCNT thin-film to a representative control sample. The control sample for Raman spectroscopy was obtained directly from CSA processing of the as-received “Ultra-Pure SWNTs” NanoIntegris paper. A second control sample, which was 80-nm-thick and with suitable transparency so that it can be used for optical absorbance spectroscopy, was fabricated from the same as-received “Ultra-Pure SWNTs” NanoIntegris paper using an MCE-based thin-film transfer method described above,<sup>27</sup> which removes surfactants from the SWCNT thin-films.<sup>26</sup> The spectra of these two control samples are labeled in Figure 2 as “As-Produced CSA” and “NI”, respectively. Figure 2(a) shows an overlay of the Raman spectra normalized to the G-band peak intensity for the as-produced CSA-film compared to the NI control sample. Also plotted in Figure 2(a) are the normalized Raman spectra for four mixed SWCNT thin-films after thermal oxidation in air at temperatures ranging from 300 °C to 425°C. Prominent differences in the Raman spectra occur as the thermal oxidation temperature is increased and the CSA is removed leading to peaks becoming sharper, more intense, and shifting towards the control sample. The as-produced CSA-film exhibits a  $G'/G$  peak ratio of 0.3, which is 40% lower than the NI control sample. The ratio

systematically increases at higher thermal oxidation temperatures, realizing the value of the NI control sample when the temperature is increased to 400 °C. Recovery of the  $G'/G$  ratio indicates that the CSA has been removed, consistent with previous work with nitric acid.<sup>8</sup> The detail of the  $G'$  suppression from CSA can be observed in Figure 2(b), where both the peak amplitude is increased and the position of the peak shifts towards the NI control sample. The optical absorbance spectra for the mixed SWCNT thin-films after thermal oxidation treatment is shown in Figure 2(c) compared to the as-produced sample and NI control. Figure 2(c) shows that the as-produced CSA-films have a suppressed  $S_{11}$  peak, which is typical of doped semiconductor and mixed films.<sup>17,19,24</sup> The  $S_{11}$  peak increases as the film is thermally oxidized, indicating removal of the acid-doping species, and reaches a maximum after the 400 °C process. The ratio between the absorbance intensity of the first ( $S_{11}$ ) and second ( $S_{22}$ ) semiconducting peaks was analyzed and compared between treatment conditions. Figure 2(d) summarizes the Raman  $G'/G$  and optical absorbance  $S_{11}/S_{22}$  ratios for the as-produced CSA-films, thermally oxidized films, and NI control sample. Ratios from both techniques recover to the control NI value after the 400 °C thermal oxidation process indicating that the thin-film has returned to the initial undoped condition. Therefore, this condition was selected to remove effects of CSA doping for all other films prior to exposure to varying dopants.

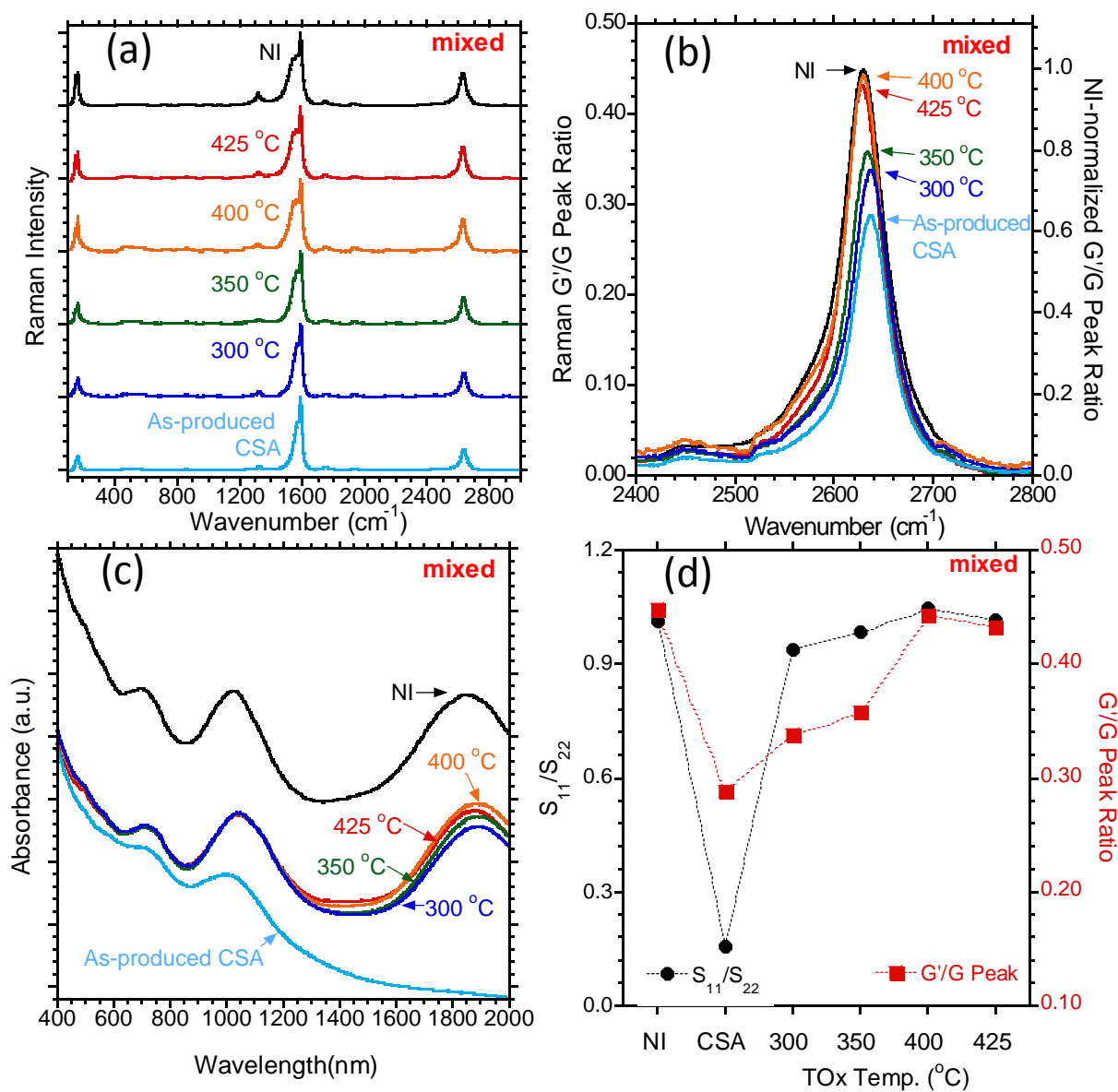


Figure 2. (a) Raman spectra of the mixed NanoIntegris SWCNT thin-film (NI), as-produced CSA-film, and after thermal oxidation at different temperatures. (b) Overlay of the G' peak for the different thermal oxidations with intensity normalized to the G-band peak intensity on the Y1 axis and normalized to the G'/G ratio of the NI control sample on the Y2 axis. (c) Overlay of optical absorbance spectra for the mixed NanoIntegris thin-film (NI), as-produced CSA-film, and after

thermal oxidation at different temperatures. (d)  $G'/G$  and  $S_{11}/S_{22}$  ratios for the different thermal oxidation (TOx) temperatures compared to CSA doped and NI control samples.

Doping susceptibility in electronic-type-separated SWCNT thin-films was performed on the purified structures to further understand the relative enhancement in conductivity and the mechanism for doping. The thin-film nanoscale surface morphology is a key parameter to ensure consistency between samples, and representative SEM micrographs are presented in Figure 3(a), (b), and (c) for the semiconducting (“semi”), mixed, and metallic-enriched SWCNT thin-films, respectively. Each of the electronic-type-separated and mixed electronic-type samples was produced using CSA, and purified with 400 °C thermal oxidation. SWCNT bundles with similar diameters are clearly visible in each of the SEM images. There appears to be some localized bundle alignment in the case of the semi and metallic SWCNTs, but the overall SWCNT film structure is randomly aligned for all cases. The observed morphology of the SWCNT thin-films by SEM is similar before the purification step (see supporting information Figure S1), suggesting that the processing is not disrupting the physical structure, but rather removing the acid from the SWCNT network.

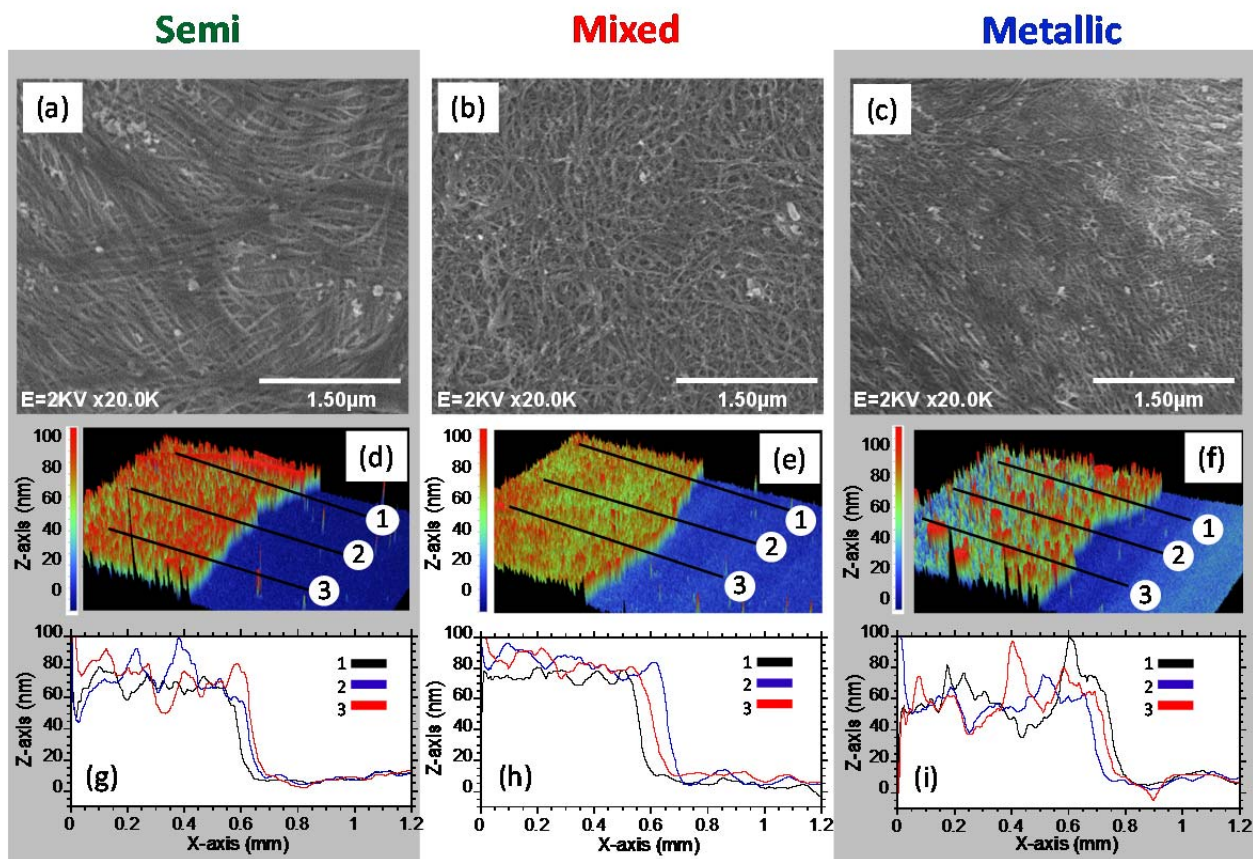


Figure 3. SEMs of purified (a) semi, (b) mixed and (c) metallic SWCNT thin-films. Optical interferometry analysis showing the 3D topology of three selected line-scan step edges for (d) semi, (e) mixed and (f) metallic SWCNT thin-films. The three representative line-scan profiles (labeled as 1, 2 and 3) from intersections through the step edge are shown for (g) semi, (h) mixed and (i) metallic thin-films, where the average thickness of the SWCNT thin-film can be quantified.

The three-dimensional SWCNT thin-film surface profile was measured by optical interferometry and is clearly observed in Figure 3(d), (e), and (f) for the semi, mixed, and metallic SWCNT thin-films, respectively. The SWCNT thin-film surface uniformity is greatest in the case of the mixed film based upon the z-axis mapping, and is visually consistent with the lack of bundle alignment observed in the SEM images. Given the characteristic nanoscale film

roughness, three discrete steps for a  $1.2 \text{ mm} \times 1.2 \text{ mm}$  sample area were used to obtain average values for film thickness as shown by the designated lines in Figure 3(d), (e), and (f). Two-dimensional line-scan profiles of the analysis step are shown in Figure 3(g), (h), and (i). The average thickness values from three representative line-scan profiles for semi SWCNT thin-films are  $70 \pm 15 \text{ nm}$ , the mixed SWCNT thin-films are  $80 \pm 10 \text{ nm}$ , and the metallic SWCNT thin-films  $60 \pm 15 \text{ nm}$ . Thus, optical interferometry represents a rapid, non-contact technique for measuring SWCNT thin-film properties and offers significant advantages over contact profilometry (typically a single narrow step on the sample that can physically damage the film during characterization) and high resolution microscopy methods such as SEM, TEM, and AFM,<sup>17</sup> which require extensive sample preparation and the measurements are performed on a small sample area. The optical interferometry analysis provides confirmation of the film quality and consistency, while also quantitatively being used to determine the thickness for each SWCNT thin-film, which is used to calculate the bulk electrical conductivity.

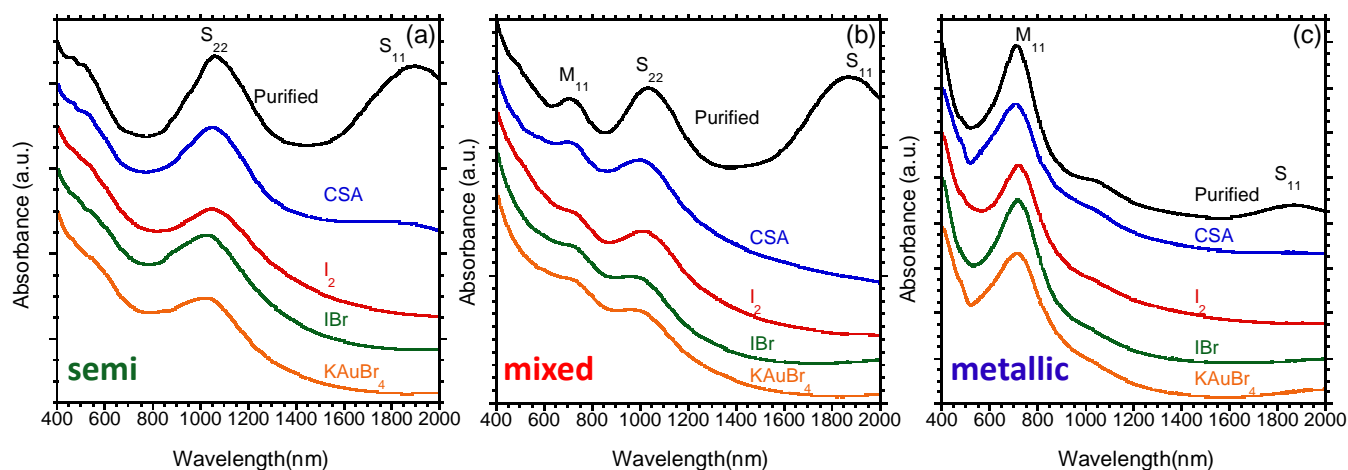


Figure 4. Overlay of optical absorbance spectra, offset for clarity, for the purified SWCNT thin-films and samples doped with CSA,  $I_2$ , IBr, and  $KAuBr_4$  for (a) semi, (b) mixed, and (c) metallic SWCNTs.

Each of the SWCNT thin-films was analyzed by optical absorption to understand the effects of chemical doping and purification on the electronic transitions for the semi, mixed, and metallic SWCNT structures. The optical absorbance of the as-produced SWCNT thin-films, labeled “CSA” on Figure 4, shows a suppressed  $S_{11}$  peak for all film types. After thermal oxidation at the established conditions from Figure 2, the  $S_{11}$  peak recovers in all films and the  $S_{22}$  peak is more pronounced. It can also be observed that the purified metallic thin-film shows a small  $S_{11}$  peak that is not present in the CSA film, which is attributed to the 2% of semiconducting content expected in this commercial material (Iso-Nanotubes-M (98%)). After doping the thin-films with  $I_2$ , IBr and  $KAuBr_4$ , a clear suppression of the  $S_{11}$  peak and a reduction of the  $S_{22}$  peak are again observed for the semi and mixed thin-films. The level of peak suppression is similar to that originally observed in the as-produced CSA thin-films, indicating reversibility of the doping process. The doping-induced suppression of the semiconductor transition peaks has been reported by other authors in electronic-type-separated SWCNT thin-films doped with  $SOCl_2$  and  $HNO_3$ ,<sup>17,19,24</sup> and is related to generation of hole carriers. In the present work,  $KAuBr_4$  presents the highest relative change in the quenching of the  $S_{11}$  peak (in Figure 4) when compared to the other dopants, suggesting that it has the strongest charge transfer interaction.

Further analysis of the peak intensities of the optical absorbance data was performed to investigate the extent of doping on the  $S_{22}$  (for semi and mixed) and the  $M_{11}$  peaks (for metallic) of the purified and doped SWCNT thin-films. Figure S2 shows that there is suppression of the  $S_{22}$  and  $M_{11}$  peaks with doping, and that  $KAuBr_4$  exhibits the most significant change for each particular electronic-type. In the case of the metallic SWCNT thin-films (see Figure 4c), the small  $S_{11}$  peak is suppressed and the dominant  $M_{11}$  transition is slightly quenched by each of the

dopants. Overall, the ability to dramatically influence the electronic transitions for semi SWCNTs compared to the metallic SWCNTs (i.e. doping effectiveness) are consistent with previous work<sup>17</sup> and show the unique response of type-separated SWCNTs.

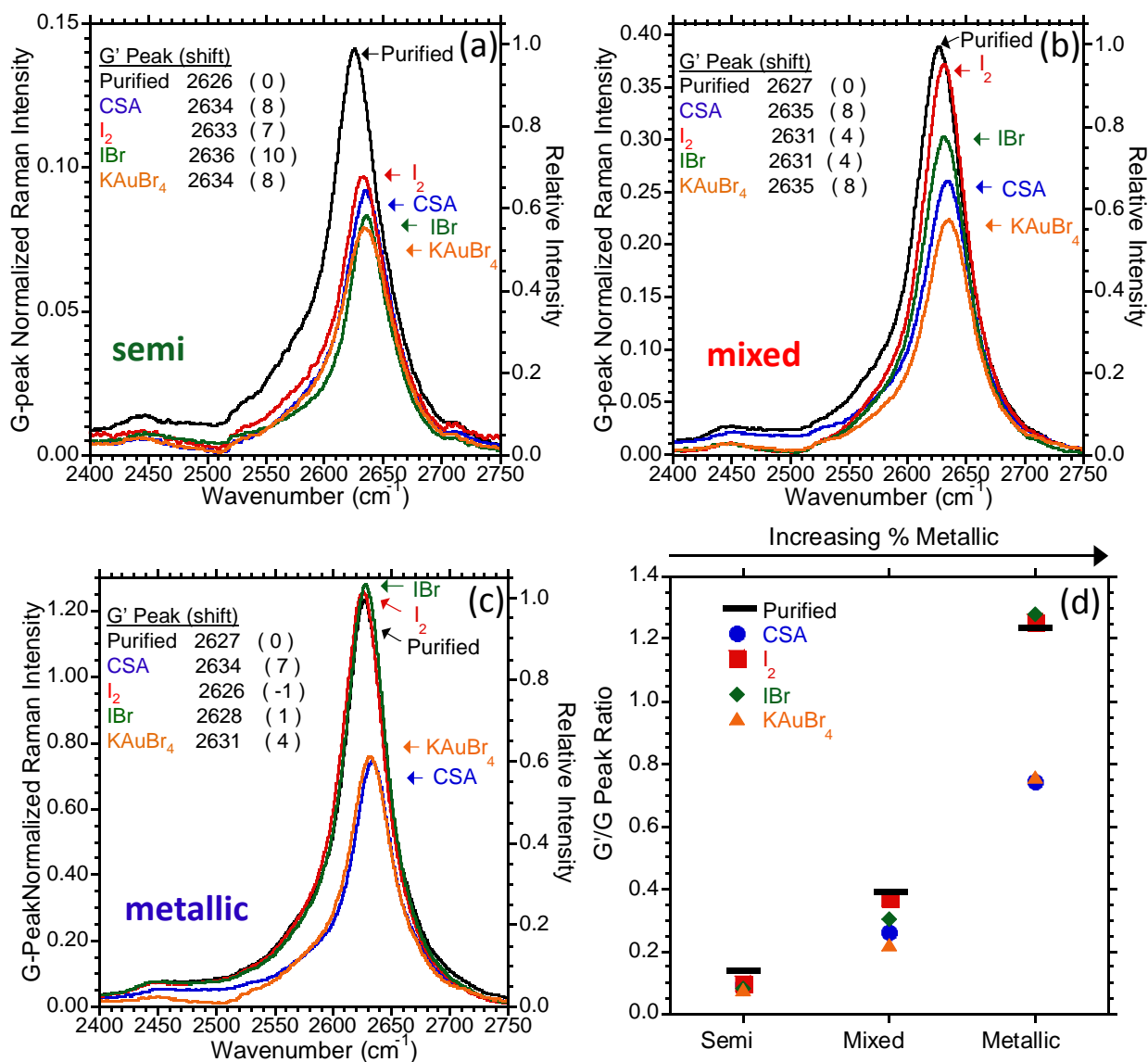


Figure 5. Overlay of the Raman G'-band, (normalized to the G-band peak intensity for each sample), for purified SWCNT thin-films and doping conditions for (a) semi, (b) mixed, and (c) metallic. The second Y-axis indicates the relative intensity change with respect to the purified samples. Inset text indicates the peak positions and respective shifts due to doping. (d) Represents

a summary of the normalized  $G'/G$  intensity peak ratio of the purified thin-films (black line) and doped samples (corresponding symbols) with varying metallic content.

Raman spectroscopy has been used to monitor physical changes in the purified and doped electronic-type-separated SWCNT thin-films (see full spectra in the supporting information Figure S3). There are characteristic changes in the prominent peak frequencies and line shapes based on the interaction between electronic-type-separated SWCNTs and the chemical dopants. The peaks in the RBM region of the doped films have been quenched with respect to those of purified films as seen in Figure S4. The G-band, shown in Figure S5, exhibits suppression of the BWF feature for the metallic SWCNTs by CSA and  $\text{KAuBr}_4$  dopants, and suggests strong interactions between chemical species and SWCNTs. Raman peak shifts for the G-band have been attributed to doping effects and have been used to approximate the number of injected carriers as well as to determine their donor or acceptor nature.<sup>22,35</sup> In general, red shifts in the Raman peaks indicate electron withdrawing (also referred to as hole doping or acceptor-type doping) based upon chemical interactions with the SWCNT resonant modes.<sup>17,35,36</sup>

Although the RBM and G-band exhibit notable changes with doping, the  $G'$ -band has been shown to be more sensitive to assess physical and chemical changes in SWCNTs due to defects, acid doping, and chemical interactions.<sup>8,16,27,37</sup> The double-resonant  $G'$ -band shows a significant modulation in amplitude relative to the other prominent peaks (*i.e.*, RBM, G-band, etc.) with varying metallic content, as shown in Figure S3 for the Raman spectra of purified electronic-type-separated SWCNT thin-films. For example, the  $G'/G$  peak ratio of purified SWCNT thin-films varies from 0.14 for semi, to 0.39 for mixed, and to 1.23 for metallic. The differences are attributed to the strong correlation in coupling between phonons and free carriers in existing electronic states for semi and metallic SWCNTs.<sup>36</sup> The normalized intensity of this resonance to

the G-band for each type, as well as the corresponding peak shifts, can be used to compare the effects of different chemical interactions with purified SWCNT thin-films. The normalized Raman intensity for the G'-band relative to the G-band for the semiconducting enriched thin-films is shown in Figure 5(a). Suppression of the normalized G' peak is observed for all dopants, with KAuBr<sub>4</sub> showing the largest response (45% suppression) followed by IBr, CSA and I<sub>2</sub> with 42%, 37% and 34% suppression, respectively. Mixed SWCNT thin-films also show the largest suppression of the G' peak intensity for KAuBr<sub>4</sub> doped thin-films (42% suppression) but with smaller responses for CSA, IBr and I<sub>2</sub> doped thin-films with 35%, 25% and 5% suppression, respectively, as shown in Figure 5(b). Metallic SWCNT thin-films show a similar suppression of 40% for the G'-peak after doping with CSA and KAuBr<sub>4</sub>, but no significant change with the I<sub>2</sub> and IBr dopants, as shown in Figure 5(c). Figure 5(d) summarizes the results for purified and doped SWCNT thin-films, where the G'/G peak ratio amplitude decreases significantly (~40%) for all electronic-types during doping except in the case of I<sub>2</sub> and IBr with mixed and metallic thin-films.

The position of the G'-band is also sensitive to Raman shifts due to chemical interactions when compared to purified samples.<sup>37</sup> Semi SWCNT thin-films show red shifts for the G'-band with all the doping chemicals: CSA (8 cm<sup>-1</sup>), I<sub>2</sub> (7 cm<sup>-1</sup>), IBr (10 cm<sup>-1</sup>) and KAuBr<sub>4</sub> (8 cm<sup>-1</sup>) when compared to the purified sample. Mixed SWCNT thin-films also show red shifts for the various dopants: CSA (8 cm<sup>-1</sup>), I<sub>2</sub> (4 cm<sup>-1</sup>), IBr (4 cm<sup>-1</sup>) and KAuBr<sub>4</sub> (8 cm<sup>-1</sup>). However, the peak shift effects are less with mixed SWCNT thin-films for I<sub>2</sub> and IBr compared to the semi SWCNT thin-films. In the case of metallic SWCNT thin-films, notable red shifts occur for CSA (7 cm<sup>-1</sup>) and KAuBr<sub>4</sub> (4 cm<sup>-1</sup>), however, the halogen dopants, I<sub>2</sub> and IBr, exhibit shifts of less than 1cm<sup>-1</sup>. The shifts of the Raman G'-band position are related to both the Fermi level change<sup>36</sup> and the

contraction/stiffening of the C-C bonds as the thin-films are doped.<sup>35,45</sup> Therefore, the observed doping of SWCNT thin-films is affected by the unique electrochemical interaction between chemical species and the SWCNT electronic-type (semi or metallic), resulting in specific peak quenching and shifts for the G'-band. Further discussion on this topic is referred to section IV.

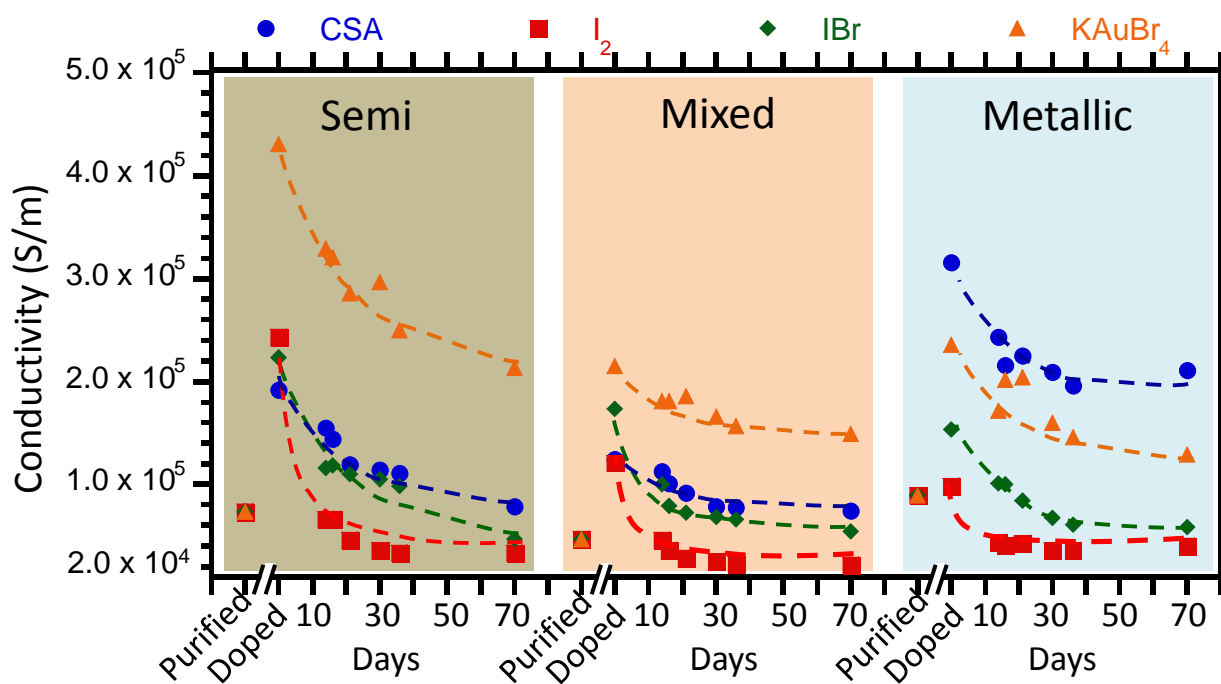


Figure 6. Electrical conductivity of semi, mixed, and metallic purified SWCNT thin-films and the corresponding effects of each dopant, including time-dependent stability. The data points should include error bars representing  $\pm 15\%$  error based on the thickness measurements, but have been omitted due to clarity.

The electrical conductivity of purified and doped electronic-type-separated SWCNT thin-films is calculated based on the sheet resistance and thickness of each sample (measurements by optical profilometry), and is presented in Figure 6. The thickness measurements include a  $\pm 15\%$  variation in conductivity due to the error in the thickness measurement, which should also

be added to each of the reported values in Figure 6, but has been omitted for clarity. The purified, semi SWCNT thin-film has an average conductivity of  $7.3 \times 10^4$  S/m based on the average of four samples, while the purified, mixed SWCNT thin-film has an average conductivity of  $4.6 \times 10^4$  S/m. The purified, metallic SWCNT thin-film has a slightly higher average conductivity compared to the other purified electronic-type-separated SWCNT thin-films at  $9.0 \times 10^4$  S/m. The relatively higher average conductivity for semi and metallic films compared to the mixed sample may be attributed to the difference in network transport from contact resistances in mixed SWCNT electronic-types.<sup>38,39</sup> The doped semi SWCNT thin-films show the largest increase in conductivity by an average of 3x with I<sub>2</sub>, IBr, and CSA, while KAuBr<sub>4</sub> resulted in a 6x increase to the highest overall conductivity of  $4.3 \times 10^5$  S/m. Metallic SWCNT thin-films show a marked change in conductivity when doped (up to 3.5x) with respect to the purified film when using CSA and KAuBr<sub>4</sub> dopants. The use of I<sub>2</sub> and IBr has minimal influence on the metallic SWCNT thin-film conductivity, which is consistent with the lack of doping changes based upon the Raman results. Mixed SWCNT thin-films exhibit a relative increase in conductivity, on average between the phase-pure semi and metallic SWCNT thin-films ranging from 3x to 5x (note the lower purified electrical conductivity of mixed SWCNT thin-films), with KAuBr<sub>4</sub> offering the largest increase. Figure S6 shows the relative change in electrical conductivity of the different electronic-type SWCNT thin-films after doping. All the data was normalized to the electrical conductivity of the respective purified sample for each SWCNT electronic-type. In general, the electrical conductivity of the doped semi SWCNT thin-films increases the most compared to the mixed and metallic SWCNT electronic-types. The metallic SWCNT thin-film doped with CSA is the one exception to this trend, where a 3.6x increase in electrical conductivity is observed compared to the 2.6x increase for the semi SWCNT sample. Although material variations in

length, defect density, and bundling are likely additional factors affecting relative changes in conductivity from inter-SWCNT barriers,<sup>17,38</sup> the present results illustrate the importance of specific chemical interactions with electronic-type-separated SWCNTs and the resulting electrical conductivity. The purified metallic SWCNT thin-film exhibits the higher intrinsic conductivity, however, the semi SWCNT thin-films show the highest susceptibility for the present dopants resulting in the largest relative change in conductivity. Although a slightly higher relative change is observed using CSA with metallic SWCNT thin-films (potentially related to the proton affinity with metallic chiralities),<sup>40</sup>  $\text{KAuBr}_4$  achieves a significant change in the electrical conductivity for all SWCNT thin-film samples and continues to represent a unique electrochemical interaction for enhancement.

The time-dependent conductivity of the SWCNT thin-films was measured by storing the doped SWCNT samples under ambient room conditions (Temperature = 18-20 °C, Relative Humidity = 20-40%) for 70 days while performing four point probe measurements to better understand dopant stability. As shown in Figure 6, the electrical conductivity of all doped SWCNT thin-films decreases over time, while the purified undoped SWCNT thin-films remained unchanged. The dashed lines are a guide to the eye to follow the decay that levels off after approximately 30 days. There is no appreciable difference in stability as a factor of the SWCNT electronic-type. On the other hand, there are appreciable differences due to the type of dopants. SWCNT thin-films doped with  $\text{I}_2$  and  $\text{IBr}$  are the least stable in all three electronic-type-separated SWCNT thin-films. The electrical conductivity of the SWCNT thin-films doped with  $\text{IBr}$  decrease back to the original undoped conductivity in about 30-40 days, while SWCNT thin-films doped with  $\text{I}_2$  result in a lower electrical conductivity 10 days after doping compared to the purified value. This result is attributed to the residual disorder that has been proposed from  $\text{I}_2$

intercalation and removal from SWCNT bundles,<sup>22</sup> resulting in additional SWCNT defects which lower the electrical conductivity. Further support for this mechanism is provided by the comparison of the Raman data in Figure S8 with Figure S3, which shows ~50% increase in the D-band for metallic SWCNT thin films doped with I<sub>2</sub> after 40 days compared to the purified SWCNT thin film, as seen in Figure S9. The electrical conductivity retention for CSA is highest for the metallic SWCNT thin-films and progressively lower for the mixed and semi SWCNT thin-films, respectively. These results are consistent with studies where mixed SWCNT films, electrochemically doped with ClO<sub>4</sub><sup>-</sup> ions, have shown a similar decrease in conductivity in a period of 30 days.<sup>41</sup> Moreover, other reports have shown that the conductivity of HNO<sub>3</sub>-doped SWCNT films decrease rapidly to an undoped value over a period of 100 hours.<sup>42</sup> However, in the case of KAuBr<sub>4</sub>, the electrical conductivity after 70 days for all three SWCNT electronic-types is still higher than the electrical conductivity of the purified thin-films, being the highest for the semi SWCNT thin-films. This is consistent with other reports in which SWCNTs doped with a metal salt, triethyloxonium hexachloroantimonate, retained 85% of their conductivity enhancement after 100 hours.<sup>42</sup>

Raman and optical absorbance spectroscopy performed on the samples 40 days after doping confirm some of the SWCNT thin-films have reversed to the purified state (*i.e.*, time-dependent de-doping). Figure S7 compares the optical absorbance data for the doped semi SWCNT thin-films immediately after doping and 40 days after doping. Both the S<sub>11</sub> and S<sub>22</sub> peaks of the IBr and I<sub>2</sub> doped semi SWCNT thin-films have recovered to the peak intensities of the purified SWCNT thin-films. The S<sub>22</sub> peak of the CSA-doped thin-film has fully recovered but the S<sub>11</sub> has only recovered moderately. Lastly, the KAuBr<sub>4</sub>-doped thin-film shows a near-complete recovery of the S<sub>22</sub> peak but only a weak recovery of the S<sub>11</sub> peak. Although thick (>50 μm) SWCNT

films have been reported to remain stable under ambient conditions below 100 °C based upon TGA data,<sup>22</sup> iodine is expected to sublime at room temperature and would need an effective encapsulation to remain within the SWCNT thin-films. In the case of semi SWCNT thin-films doped with CSA and KAuBr<sub>4</sub>, the measured electrical conductivity retention after 40 days is consistent with the persistent quenching of the S<sub>11</sub> peak in the optical absorbance spectra in Figure S7 indicative of stronger, more stable chemical interactions.

The Raman G'-band has been used to monitor doping retention in the metallic SWCNT thin-films since no significant modulation of the M<sub>11</sub> was observed in the optical spectra for doped samples. Figure S8 shows the full Raman spectra of the doped metallic SWCNT thin-films 40 days after doping compared to the purified samples. Figure S9 shows a summary of the G' peak normalized to the G-peak as an indicator of doping stability for the metallic SWCNT thin-films. The samples doped with I<sub>2</sub> and IBr, shown in Figure S9(b) and (c) respectively, remain unchanged in terms of not interacting with the metallic SWCNT thin-films, as observed with the purified SWCNT thin-film. In comparison, the G' peak intensity for the metallic SWCNT thin-films doped with CSA and KAuBr<sub>4</sub> show some recovery but persistent suppression of the G' peak after 40 days, as seen in Figure S9(a) and (d). Thus, the Raman results indicate that the effects of these dopants have been preserved in ambient conditions, allowing for the enhanced conductivity to remain. Collectively across all samples, the time-dependent doping results indicate that it is essential that encapsulation strategies be pursued to maintain enhanced conductivity in SWCNT thin-films based upon chemical doping for practical applications.

#### IV. Discussion

The effectiveness of certain chemical dopant interactions with electronic-type-separated SWCNTs is shown to be critical to enhance the electrical conductivity. The results from optical

absorbance and Raman spectroscopy show clear interactions between the chemical dopants and type-separated SWCNTs. The sensitivity of the Raman G' peak with doping can be used to correlate the relative change in the electrical conductivity of SWCNT thin-films to the G' peak shift after doping. Figure 7(a) summarizes the data for each of the measured SWCNT thin-films and shows that the largest shift in the Raman G' peak correlates with the largest improvement in electrical conductivity and can be an empirical relationship for determining the extent of charge transfer. For the semi and mixed SWCNT thin-films (triangle and circle symbols in Figure 7(a), respectively), the relationship between the G'-peak shift and the relative change in conductivity is loosely distributed between  $4 - 10 \text{ cm}^{-1}$  and 2.5x to 6.0x, respectively. This threshold doping behavior suggests an underlying relationship with the quantized electronic states for semi SWCNTs based on their bandgaps and requires a sufficient electrochemical difference to activate a response. A scattered response is observed above the activation potential due to other factors, such as intercalated dopants, local redox potential variations, and chemical interactions at higher electronic states (i.e. S<sub>22</sub>, S<sub>33</sub>, etc.) For the metallic SWCNT thin-films, a linear relationship is observed between the G'-peak shift and the relative conductivity increase (square symbols in Figure 7 (a)), indicating a gradual increase in doping efficacy based on minimal depletion of electron density from chemicals with a lower redox potential and significant depletion of electron density (potentially including the M<sub>11</sub> band) from chemicals with higher redox potential.

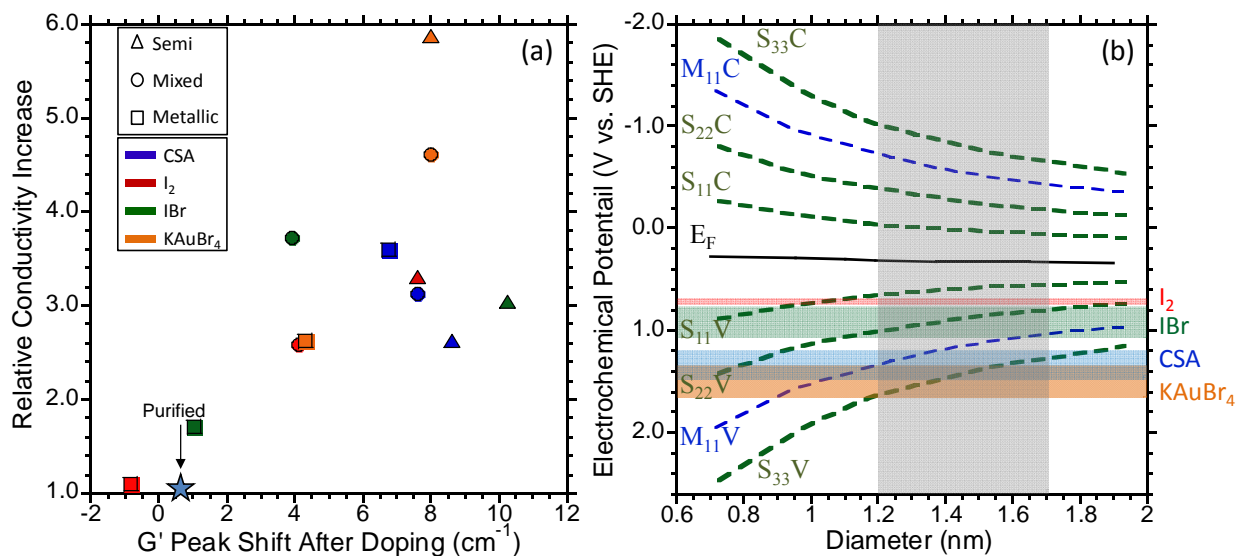


Figure 7. Relative change in electrical conductivity as a function of the G'-peak position shift based upon the ratio of the electrical conductivity of the doped to purified SWCNT thin-film. (b) Fermi level position and electrochemical potential of the valence (V) and conduction (C) energy transitions, with respect to a standard hydrogen electrode, as a function of SWCNT diameter.<sup>20</sup> The range of redox potentials of the doping species and the range of SWCNT diameters in this experiment (1.2 – 1.7 nm) is represented by the shaded regions.<sup>46</sup>

Figure 7(b) shows the valence and conduction energy levels of SWCNTs as a function of their diameter with respect to a standard hydrogen electrode (SHE) to relate the electrochemical potential for the SWCNTs and the doping species involved in these experiments.<sup>43,44,20</sup> Thus, it can be seen that the redox potentials of all four dopants have a more positive potential than the energy of the first semiconducting electronic transition, indicating that all four dopants can oxidize the semiconducting SWCNTs. There is some uncertainty in terms of the exact redox potential for some of the doping species given the complex reaction in solution and this is represented by the bands in Figure 7(b). Since the semi SWCNT thin-films contain the highest concentration of semiconducting SWCNTs compared to the mixed thin-films, it explains the

greater  $G'$ -peak shifts for these samples and corresponding higher electrical conductivities. In some cases, the redox potential of certain doping species could exceed the second and third semiconducting transition energy levels. As indicated by Figure 7(b), this may explain the dramatically higher doping response with  $\text{KAuBr}_4$  due to the more positive electrochemical potential, suggesting that the  $S_{33}$  is also being depleted of electron density. In comparison, the electrical conductivity improvement of metallic SWCNT thin-films, based on the shift of the  $G'$  peak position, is gradual and continuous (square symbols in Figure 7 (a)). This correlates to the fact that the first metallic SWCNT electronic transition band is at a much higher energy than the observed Fermi level and the interaction with chemical dopants can take place gradually with the available density of states present in the low energy levels.<sup>45</sup>  $\text{I}_2$  and  $\text{IBr}$  dopants weakly dope the metallic SWCNTs due to the fact that the redox potential of the doping species tend to be less positive than the first metallic SWCNT electronic transition with a diameter range of 1.2 - 1.7 nm.<sup>20,46</sup> Conversely, CSA and  $\text{KAuBr}_4$  result in strongly doped metallic SWCNT films as the redox potential of the dopant species (*i.e.*,  $\text{ClO}_4^-$ ,  $\text{Au}_3^+$ ,  $\text{Au}^+$ ) are near or more positive than the first metallic SWCNT electronic transition.<sup>46</sup>

The combination of the spectroscopy results (*e.g.*, optical absorption suppression and Raman  $G'$  peak intensity and shifts) with the electrical conductivity measurements supports the mechanism of electrochemical doping for SWCNTs. Based upon the equilibrium redox potentials, the strength of an acceptor-dopant to oxidize the SWCNTs will be based on the alignment of the electrochemical potential with a specific SWCNT electronic-type. In the case of the present four dopants, CSA and  $\text{KAuBr}_4$  are most effective across all samples due to the more positive electrochemical potential whereas  $\text{I}_2$  and  $\text{IBr}$  are only effective with semi SWCNT thin-films due to their corresponding lower potential. Thus, the number of chemical species

available to dope semi SWCNT thin-films will be greater compared to metallic SWCNT thin-films due to the larger potential needed to exceed the  $M_{11}$  transition energy. The observed trend in Figure 7(a) is that higher conductivity results when significant doping occurs measured by Raman shifts in the  $G'$  peak. This result suggests that the chemical dopants are primarily affecting the intra-SWCNT and intra-SWCNT bundle transport since the Raman data will be largely probing the intrinsic SWCNT properties. There is some scatter in the data for the mixed SWCNT samples, which is attributed to the overall transport variability in contact resistance modification to the semi and metallic SWCNT junction sites affecting the inter-SWCNT transport (as measured previously by conductive AFM).<sup>39</sup> Overall, the results herein demonstrate that using highly enriched electronic-type-separated SWCNTs support the past theoretical predictions and results with mixed SWCNTs<sup>20</sup> and substantiate the mechanism of electrochemical doping in SWCNTs towards providing a predictive framework for advancing the electrical conductivity in bulk structures.

## V. Conclusions

A comprehensive study of chemical dopants has shown that alkali gold halides, gold halides, iodine-based halides and acid solutions are the most efficient at increasing the conductivity of purified CNT films by up to 8x. The best performing dopants (*i.e.*,  $I_2$ , IBr, CSA and  $KAuBr_4$ ) have been used to further investigate changes in the optical absorption, Raman spectra and electrical conductivity of electronic-type-separated SWCNT thin-films. A method was developed to purify SWCNT thin-films by removing the CSA dispersant through thermal oxidation. The thickness of the SWCNT thin-films, which is critical when measuring electrical conductivity, was rapidly and accurately measured using a non-contact optical interferometry method. Quenching of the  $S_{11}$  and  $S_{22}$  absorption bands and shifts and quenching of the Raman  $G'$  peak

indicate electron withdrawal from the semiconducting SWCNT thin-films. On the other hand, doped metallic SWCNT thin-films do not show significant quenching of the  $M_{11}$  optical absorption peak, but a gradual quenching and shift of the Raman  $G'$  peak that correlates to a similar linear increase in electrical conductivity based on the dopant type. The difference in doping behavior between semiconducting and metallic films is explained by the redox potential of the doping species and how they compare to the position of the SWCNT metallic and semiconducting transition energies. The results of this work present an improved validation of the doping mechanism of electronic-type-separated SWCNTs as a function of the redox potential of doping species, and provide a path towards enhancing the electrical conductivity of carbon nanotubes that can enable their implementation in a variety of wire and cable applications traditionally employed by metals.

#### **ELECTRONIC SUPPLEMENTARY INFORMATION**

SEM analysis of as produced and purified semi, mixed and metallic SWCNT thin-films; optical absorbance spectra detail of normalized  $S_{22}$  or  $M_{11}$  peak of purified and doped SWCNT thin-films; full Raman spectra and detail of RBM and G-band of doped semi, mixed and metallic SWCNT thin-films; relative change in electrical conductivity of doped semi, mixed and metallic SWCNT thin-films; comparison of optical absorbance spectra of doped semi SWCNT thin-films and after 40 days; full Raman spectra of doped metallic SWCNT thin-films after 40 days; comparison of Raman D-band of doped metallic SWCNT thin-films as doped and after 40 days; detail of normalized Raman  $G'/G$  band of SWCNT metallic thin-films as doped and after 40 days.

#### **AUTHOR INFORMATION**

##### **Corresponding Author**

\*Brian Landi, Lomb Memorial Drive, Rochester, NY 14623. USA

### Author Contributions

The manuscript was written through contributions of all authors. / All authors have given approval to the final version of the manuscript.

### ACKNOWLEDGMENT

This project was partially supported by a grant from the Intelligence Community Postdoctoral Research Fellowship Program through funding from the Office of the Director of National Intelligence. The authors also acknowledge funding from the U.S. Government, the Defense Threat Reduction Agency (DTRA) under Grant HDTRA-1-10-1-0122, and the Air Force Research Laboratory under agreement number FA9453-14-1-0232. All statements of fact, opinion, or analysis expressed are those of the author and do not reflect the official positions or views of the Intelligence Community or any other U.S. Government agency. Nothing in the contents should be construed as asserting or implying U.S. Government authentication of information or Intelligence Community endorsement of the author's views.

### REFERENCES

1. P. Jarosz, C. Schauerma, J. Alvarenga, B. Moses, T. Mastrangelo, R. Raffaele, R. Ridgley and B. Landi, *Nanoscale*, 2011, **3**, 4542.
2. N. Behabtu, C. C. Young, D. E. Tsentelovich, O. Kleinerman, X. Wang, A. W. K. Ma, E. A. Bengio, R. F. ter Waarbeek, J. J. de Jong, R. E. Hoogerwerf, S. B. Fairchild, J. B. Ferguson, B. Maruyama, J. Kono, Y. Talmon, Y. Cohen, M. J. Otto and M. Pasquali, *Science* (80-. ),, 2013, **339**, 182–6.
3. J. Alvarenga, P. R. Jarosz, C. M. Schauerma, B. T. Moses, B. J. Landi, C. D. Cress and R. P. Raffaele, *Appl. Phys. Lett.*, 2010, **97**, 2010–2012.

4. H. Dai, *Surf. Sci.*, 2002, **500**, 218–241.
5. B. J. Landi, R. P. Raffaele, M. J. Heben, J. L. Alleman, W. VanDerveer and T. Gennett, *Mater. Sci. Eng. B Solid-State Mater. Adv. Technol.*, 2005, **116**, 359–362.
6. R. P. Raffaele, B. J. Landi, J. D. Harris, S. G. Bailey and a. F. Hepp, *Mater. Sci. Eng. B*, 2005, **116**, 233–243.
7. D. Chattopadhyay, I. Galeska and F. Papadimitrakopoulos, *J. Am. Chem. Soc.*, 2003, **125**, 3370–3375.
8. B. J. Landi, C. D. Cress, C. M. Evans and R. P. Raffaele, *Chem. Mater.*, 2005, **17**, 6819–6834.
9. K. Yanagi, H. Udoguchi, S. Sagitani, Y. Oshima, T. Takenobu, H. Kataura, T. Ishida, K. Matsuda and Y. Maniwa, *ACS Nano*, 2010, **4**, 4027–4032.
10. J. H. Jang, S. C. Lim, D. L. Duong, G. Kim, W. J. Yu, K. H. Han, Y.-S. Min and Y. H. Lee, *J. Nanosci. Nanotechnol.*, 2010, **10**, 3934–3939.
11. M. a. Kanygin, O. V. Sedelnikova, I. P. Asanov, L. G. Bulusheva, a. V. Okotrub, P. P. Kuzhir, a. O. Plyushch, S. a. Maksimenko, K. N. Lapko, a. a. Sokol, O. a. Ivashkevich and P. Lambin, *J. Appl. Phys.*, 2013, **113**.
12. F. Villalpando-Paez, a. Zamudio, a. L. Elias, H. Son, E. B. Barros, S. G. Chou, Y. a. Kim, H. Muramatsu, T. Hayashi, J. Kong, H. Terrones, G. Dresselhaus, M. Endo, M. Terrones and M. S. Dresselhaus, *Chem. Phys. Lett.*, 2006, **424**, 345–352.
13. Y. Zhao, J. Wei, R. Vajtai, P. M. Ajayan and E. V Barrera, *Sci. Rep.*, 2011, **1**, 83.
14. D. Janas, A. P. Herman, S. Boncel and K. K. K. Koziol, *Carbon*, 2014, **73**, 225–233.
15. T. Michel, L. Alvarez, J.-L. Sauvajol, R. Almairac, R. Aznar, O. Mathon, J.-L. Bantignies and E. Flahaut, *J. Phys. Chem. Solids*, 2006, **67**, 1190–1192.

16. N. D. Cox, J. E. Rossi, C. D. Cress, A. Merrill, K. R. Crompton and B. J. Landi, *J. Phys. Chem. C*, 2014, **118**, 14031–14038.
17. J. L. Blackburn, T. M. Barnes, M. C. Beard, Y. Kim, C. Robert, T. J. McDonald, B. To, T. Coutts and M. J. Heben, *ACS Nano*, 2008, **2**, 1266–1274.
18. K. S. Mistry, B. a. Larsen, J. D. Bergeson, T. M. Barnes, G. Teeter, C. Engtrakul and J. L. Blackburn, *ACS Nano*, 2011, **5**, 3714–3723.
19. T. M. Barnes, J. L. Blackburn, J. van de Lagemaat, T. J. Coutts and M. J. Heben, *ACS Nano*, 2008, **2**, 1968–1976.
20. K. K. Kim, S.-M. Yoon, H. K. Park, H.-J. Shin, S. M. Kim, J. J. Bae, Y. Cui, J. M. Kim, J.-Y. Choi and Y. H. Lee, *New J. Chem.*, 2010, **34**, 2183.
21. S. M. Kim, K. K. Kim, Y. W. Jo, M. H. Park, S. J. Chae, D. L. Duong, C. W. Yang, J. Kong and Y. H. Lee, *ACS Nano*, 2011, **5**, 1236–1242.
22. L. Grigorian, K. A. Williams, S. Fang, G. U. Sumanasekera, A. L. Loper, E. C. Dickey, S. J. Pennycook and P. C. Eklund, *Phys. Rev. Lett.*, 1998, **80**, 5560–5563.
23. A. M. Rao, P. C. Eklund, S. Bandow, A. Thess and R. E. Smalley, *Nature*, 1997, **388**, 257–259.
24. R. K. Jackson, A. Munro, K. Nebesny, N. Armstrong and S. Graham, *ACS Nano*, 2010, **4**, 1377–1384.
25. C. M. Schauerman, J. Alvarenga, J. Staub, M. W. Forney, R. Foringer and B. J. Landi, *Adv. Eng. Mater.*, 2015, **17**, 76–83.
26. Z. Wu, Z. Chen, X. Du, J. M. Logan, J. Sippel, M. Nikolou, K. Kamaras, J. R. Reynolds, D. B. Tanner, A. F. Hebard and A. G. Rinzler, *Science*, 2004, **305**, 1273–1276.

27. J. E. Rossi, C. D. Cress, A. R. Helenic, C. M. Schauerman, R. a. Dileo, N. D. Cox, S. R. Messenger, B. D. Weaver, S. M. Hubbard and B. J. Landi, *J. Appl. Phys.*, 2012, **112**.
28. F. M. Smits, *Bell Syst. Tech. J.*, 1958, **37**, 711–718.
29. P. G. Collins, K. Bradley, M. Ishigami and A. Zettl, *Science*, 2000, **287**, 1801–1804.
30. D. J. Mowbray, C. Morgan and K. S. Thygesen, *Phys. Rev. B*, 2009, **79**, 195431.
31. D. S. Hecht, A. M. Heintz, R. Lee, L. Hu, B. Moore, C. Cucksey and S. Risser, *Nanotechnology*, 2011, **22**, 075201.
32. Y. Miyata, K. Yanagi, Y. Maniwa and H. Kataura, *J. Phys. Chem. C*, 2008, **112**, 3591–3596.
33. G. U. Sumanasekera, J. L. Allen, S. L. Fang, a. L. Loper, a. M. Rao and P. C. Eklund, *J. Phys. Chem. B*, 1999, **103**, 4292–4297.
34. P. C. Eklund, E. T. Arakawa, J. L. Zarestky, W. A. Kamitakahara and G. D. Mahan, *Synth. Met.*, 1985, **12**, 97–102.
35. A. Das, S. Pisana, B. Chakraborty, S. Piscanec, S. K. Saha, U. V Waghmare, K. S. Novoselov, H. R. Krishnamurthy, A. K. Geim, A. C. Ferrari and A. K. Sood, *Nat. Nanotechnol.*, 2008, **3**, 210–215.
36. M. S. Dresselhaus, G. Dresselhaus, a. Jorio, a. G. Souza Filho and R. Saito, *Carbon N. Y.*, 2002, **40**, 2043–2061.
37. B. J. Landi, C. M. Evans, J. J. Worman, S. L. Castro, S. G. Bailey and R. P. Raffaele, *Mater. Lett.*, 2006, **60**, 3502–3506.
38. M. A. Topinka, M. W. Rowell, D. Goldhaber-Gordon, M. D. McGehee, D. S. Hecht and G. Gruner, *Nano Lett.*, 2009, **9**, 1866–1871.
39. M.S. Fuhrer, J. Nygard, L. Shih, M. Forero, Y.-G. Yoon, M. S. C. Mazzoni, H. J. Choi, J. Ihm, S. G. Louie, and P. L. McEuen, *Science*, 2000, **288**, 494-497.

40. M. S. Strano, C. B. Huffman, V. C. Moore, M. J. O. Connell, E. H. Haroz, J. Hubbard, M. Miller, K. Rialon, C. Kittrell, S. Ramesh, R. H. Hauge and R. E. Smalley, *J. Phys. Chem. B*, 2003, **107**, 6979–6985.
41. C.-S. Park, C. J. Lee and E. K. Kim, *Phys. Chem. Chem. Phys.*, 2015, **17**, 16243–16245.
42. B. Chandra, A. Afzali, N. Khare, M. M. El-Ashry and G. S. Tulevski, *Chem. Mater.*, 2010, **22**, 5179–5183.
43. J. Zhao, J. Han and J. P. Lu, *Phys. Rev. B*, 2002, **65**, 193401.
44. [http://www.photon.t.u-tokyo.ac.jp/~maruyama/kataura/1D\\_DOS.html](http://www.photon.t.u-tokyo.ac.jp/~maruyama/kataura/1D_DOS.html) (accessed March 20, 2015).
45. W. Zhou, J. Vavro, N. Nemes, J. Fischer, F. Borondics, K. Kamarás and D. Tanner, *Phys. Rev. B*, 2005, **71**.
46. D. R. Lide, *CRC Handbook of Chemistry and Physics* (87th ed.). Boca Raton, FL: CRC Press. ISBN 0-8493-0487-3.
47. S. Costa, *Acta Phys. Pol. A*, 2009, **116**, 32–35.

Insert Table of Contents artwork here

